

pubs.acs.org/ICTC Article

Assessing the Reliability of Truncated Coupled Cluster Wave Function: Estimating the Distance from the Exact Solution

Adám Ganyecz,* Zsolt Benedek, Klára Petrov, Gergely Barcza, András Olasz, Miklós A. Werner, and Ors Legeza



Cite This: https://doi.org/10.1021/acs.jctc.5c00750



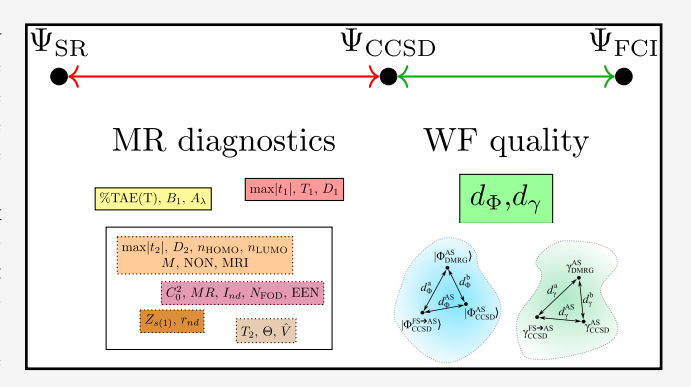
ACCESS I

III Metrics & More

Article Recommendations

Supporting Information

ABSTRACT: A new approach is proposed to assess the reliability of the truncated wave function methods by estimating the deviation from the full configuration interaction (FCI) wave function. While typical multireference diagnostics compare some derived property of the solution with the ideal picture of a single determinant, we try to answer a more practical question: how far is the solution from the exact one. Using the density matrix renormalization group (DMRG) method to provide an approximate FCI solution for the self-consistently determined relevant active space, we compare the low-level CI expansions and onebody reduced density matrixes to determine the distance of the two solutions (d_{Φ}, d_{γ}) . We demonstrate the applicability of the approach for the CCSD method by benchmarking on the W4-



17 data set, as well as on transition-metal-containing species. We also show that the presented moderate-cost, purely wave functionbased metric is truly unique in the sense that it does not correlate with any popular multireference measures. We also explored the usage of CCSD natural orbitals $(d_{\gamma,NO})$ and its effect on the active space size and the metric. The proposed diagnostic can also be applied to other wave function approximations, and it has the potential to provide a quality measure for post-Hartree-Fock procedures in general.

1. INTRODUCTION

In computational quantum chemistry, correlation effects are often distinguished into dynamic and static correlations according to their character. The latter one, also known as nondynamic correlation, can be further divided to Type A or left-right strong correlation and Type B or angular strong correlation.^{2,3} Type A correlation occurs when there is an absolute near-degeneracy, for example, bond stretching, while Type B refers to relative near-degeneracy when the gap is small compared to the orbital energies.

When dynamic correlation dominates, the routinely applied single reference (SR) quantum chemical methods, such as density functional theory (DFT) or the gold standard coupled cluster singles, doubles, and perturbative triples (CCSD(T)), work well. However, they often do not provide accurate results for molecules with a significant nondynamic correlation.^{4,5} Therefore, measuring or at least estimating the degree of correlation is a crucial point in choosing the appropriate methodology. From the practical point of view in computational chemistry, it is also required that the cost of such a measurement should be comparable to that of a single reference calculation.

To address this issue, numerous multireference (MR) diagnostics appeared in the literature 7-9 that attempt to predict the validity of the single-reference approach by analyzing the SR results themselves. Only two of them are based on CI coefficients (c_i) : $C_0^{210,11}$ is the weight of the leading determinant, usually from a CASSCF or CASCI calculation, while MR^{12} uses the second and fourth power of c_i coefficients to determine the deviation from the single determinant wave function.

Specifically, for CC methods, the most straightforward metrics were the maximum of t_1 singles and t_2 doubles amplitudes, which were available in the early versions of ACES quantum chemical program suite. 13,14 The well-known T_1^{15} and D_1^{16-18} are based on the Euclidean and the Frobenius norm of t_1 singles organized into the appropriate vector and matrix, respectively. Double excitation amplitudes can be used in a similar manner to obtain T_2^{19} and D_2^{20} for closed-shell systems. Most recently, the S diagnostic was proposed, which

Received: May 9, 2025 Revised: August 15, 2025 Accepted: August 20, 2025



Table 1. List of MR Diagnostics Studied in This Work

name	type	definition ^a	this work b	ref
C_0^2	CI coefficient	square of coefficient of leading determinant	CCSD, DMRG	10, 11
MR	CI coefficient	$\sum_{i} c_{i} ^{2} - c_{i} ^{4}$	CCSD, DMRG	12
$\max t_1 $	CC amplitudes	maximum of t_1 amplitudes	CCSD	13
$\max t_2 $	CC amplitudes	maximum of t_2 amplitudes	CCSD	13
T_1	CC amplitudes	$\ t_1\ _F/\sqrt{n_{\mathrm{corr}}}$	CCSD	15
T_2	CC amplitudes	$ t_2 _F / \sqrt{n_{\text{corr}}}$	CCSD	19
D_1	CC amplitudes	$\ \mathbf{T}_1\ _2$	CCSD	16-18
D_2	CC amplitudes	$\max(\ \mathbf{T}_2^o\ _2,\ \mathbf{T}_2^v\ _2),\text{where}\mathbf{T}_2^o\in\mathbb{R}^{ov^2\times o}\text{and}\mathbf{T}_2^v\in\mathbb{R}^{o^2v\times v}$	CCSD	20
n_{HOMO}	occupation numbers	occupation number of HOMO	CCSD, DMRG, FT-DFT	8, 22, 23
$n_{ m LUMO}$	occupation numbers	occupation number of LUMO	CCSD, DMRG, FT-DFT	8, 22, 23
M	occupation numbers	$\frac{1}{2} \left(2 - n_{\text{HOMO}} + n_{\text{LUMO}} + \sum_{j}^{N_{\text{SOMO}}} n_{j} - 1 \right)$	CCSD, DMRG, FT-DFT	22
I_{nd}	occupation numbers	$rac{1}{2}\sum_{\sigma,i}n_i^\sigma(1-n_i^\sigma)$	CCSD, DMRG, FT-DFT	25, 26
$r_{ m nd}$	occupation numbers	$\frac{\frac{1}{2}\sum_{\sigma,i}n_i^\sigma(1-n_i^\sigma)}{\frac{1}{4}\sum_{\sigma,i}(n_i^\sigma(1-n_i^\sigma))^{1/2}}$	CCSD, DMRG, FT-DFT	41
Θ	occupation numbers	$1-rac{1}{n}\sum_{i,\sigma}n_i^{\sigma 2}$	CCSD, DMRG, FT-DFT	19, 24
$N_{ m FOD}$	occupation numbers	$\sum_{i}^{N_{ m occ}} 1 - n_{i}^{\;\sigma} + \sum_{j}^{N_{ m virt}} n_{j}^{\;\sigma}$	CCSD, DMRG, FT-DFT	27, 28
EEN	occupation numbers	$\sum_i^{N_{ m virt}} n_i^{\sigma}$	CCSD, DMRG, FT-DFT	29
Ŷ	occupation numbers	$\frac{1}{n}(\sum_{i}^{N_{\mathrm{occ}}}n_{i}^{\sigma}-\sum_{i}^{N_{\mathrm{occ}}}n_{i}^{\sigma^{2}})$	CCSD, DMRG, FT-DFT	29
MRI	occupation numbers	MRI = -tanh(4.016 + log(I))	CCSD, DMRG, FT-DFT	29
		$I = \sum_{i} \exp(-1500 \times (0.5 - n_i)^6)$		
NON	occupation numbers	largest occupation number on unoccupied natural orbitals	CCSD, DMRG, FT-DFT	29
$Z_{s(1)}$	orbital entropy	$rac{1}{N\ln 4}\sum_{i}^{N}s_{i}(1)$	CCSD, DMRG	33
%TAE(T)	energy	$100 \times \frac{\text{TAE[CCSD(T)]} - \text{TAE[CCSD]}}{\text{TAE[CCSD]}}$	CCSD(T)	34, 35
B_1	energy	$\frac{\text{TAE[BLYP]} - \text{TAE[B1LYP]}}{n_{\text{bonds}}}$	BLYP, B1LYP	36
A_λ	energy	$\frac{100}{\lambda} \frac{\text{TAE}[\text{XC}] - \text{TAE}[\text{X}_{\lambda}C]}{\text{TAE}[\text{XC}]}$	PBE, PBE0	8

 ^{a}N (N_{occ} N_{virt} N_{SOMO}): number of orbitals (occupied, virtual, single occupied), $n_{(\text{corr})}$: number of (correlated) electrons, n_{i} (n_{i}^{σ} n_{HOMO} , n_{LUMO}): occupational number (spinorbitals, HOMO, LUMO) c_{i} : CI coefficient, t_{1} , t_{2} : single/double excitation CC amplitudes, TAE: total atomization energy. b Calculations used in this work to determine the metric.

also uses Lagrange multipliers in addition to the cluster amplitudes. 21

Another class of metrics is based on occupation numbers, usually of natural orbitals, which can be obtained by various methods. The simplest example uses the occupation number of HOMO and LUMO, 8,22,23 which can be combined in one number, M.²² Coe and Paterson (based on Löwdin) defined O, which indicates how far the wave function is from the singledeterminant solution of Hartree-Fock. 19,24 Ramos-Cordoba et al. derived $I_{\rm nd}$ and $I_{\rm d}$ nondynamic and dynamic correlation indices based on the two-particle cumulant matrix. 25,26 Kesharwani and co-workers defined an intensive quantity, r_{nd} , as a ratio of nondynamic and total correlation indices, $I_{\rm nd}/(I_{\rm nd}$ + $I_{\rm d}$). Grimme and Hansen^{27,28} proposed a function called fractional occupation number weighted density (FOD) to visualize static or nondynamic correlation in the molecule. Its spatial integration produces a single number that can be used as an MR diagnostic metric. The fractional occupational numbers are determined with finite-temperature DFT in this approach. Bartlett et al.²⁹ defined several new metrics for CC based on natural orbital occupation numbers, determined from 1-body RDM, but these definitions can also be used with any occupation number. The external electron number (EEN) shows how many electrons are in the virtual orbitals; its

counterpart, the variance relative to the ideal single determinant case, \hat{V} , is based on the occupation numbers of occupied orbitals and scaled with the number of orbitals. NON is the largest occupation number on unoccupied natural orbitals, which is also closely related to the LUMO occupation number. They also constructed a multireference index (MRI), transforming the occupation numbers to a single number ranging from -1 to 1, where MRI around -1 suggests MR character, while around +1 SR character is expected.

Following the work of Legeza and Sólyom on single orbital entropies³⁰ and their sum providing total correlation³¹ Boguslawski and co-workers used these concepts to study multireference nature of strongly correlated molecules.³² Later, Stein and Reiher used total correlation to define $Z_{s(1)}$ diagnostic which scales so that the maximal entanglement refers to 1 while no entanglement refers to the value 0.³³

The next group of metrics can be called energy-based multireference diagnostics. These use some ratio of total atomization energies. %TAE(T)^{34,35} measures the effect of perturbative triples on total atomization energy. B_1^{36} uses the energy difference of BLYP^{37,38} and B1LYP³⁹ and scales with the number of bonds. A_{λ}^{8} takes the difference between the pure and its hybrid DFT version and is scaled with λ , which is a percent of the HF-exchange of the hybrid functional.

Recently, Martin and his co-workers proposed ${\rm \%TAE_{X}}^{40}$ which measures for a given HF density the difference of the DFT and HF exchange energies. The various multireference diagnostics used in this work are summarized in Table 1.

Even though numerous diagnostics exist, their accuracy in predicting which system should not be handled with single reference methods is often questionable. Usually, they do not even correlate with each other. ^{6,8,40} This leads to arbitrary rules where multiple diagnostics are used, such as species with 3d transition metals are considered multireference if $T_1 > 0.05$, $D_1 > 0.15$, and %TAE[(T)] > 10%.

All of the aforementioned metrics try to determine the degree of multireference character by taking the ideal single reference wave function and measuring the deviation from it. However, the real question is how far the solution of a given method is from the exact full CI wave function.

In this work, we propose a new family of metrics, \tilde{d} , which represents the quality of the wave function by measuring its deviation from the reference obtained by high-level theory. \tilde{d}_{Φ} uses CI-coefficients up to double excitations, while \tilde{d}_{γ} uses the 1-body reduced density matrix, and $\tilde{d}_{\gamma,\mathrm{NO}}$ uses also the natural orbital transformation to reduce the size of the active space used. First, we present the formulation of the new metrics. Then, we show the validity of the introduced approximations. After that, we compare the performance of \tilde{d} -s to other popular multireference diagnostics on the W4–17 data set, and also, a grouping of existing metrics is presented. The performance is also demonstrated on transition metal species, which are particularly difficult cases for standard single reference methods.

2. THEORY

In this section, we present how the new metrics are formulated. First, we discuss the reference used and then which property will be used as a basis of comparison. After that we discuss the orbital selection procedure and then present the definition of the final metric.

2.1. Reference. Testing the quality of approximate quantum chemical methods, such as coupled cluster theory, against the exact reference provided by FCI is possible up to only 20 orbitals due to its computational demand.⁴² To overcome this limitation, in this paper, we applied the density matrix renormalization group (DMRG) approach⁴³ as a robust quasi-FCI solver with polynomial scaling. The reference for all the investigated quantities was derived from the high-precision DMRG wave function whose accuracy was controlled by the truncation error.⁴⁴ For a practical review of the DMRG method, see refs 45–53.

2.2. Basis of Comparison. There are numerous ways to compare wave functions. The easiest way would be to use energy or some other property. However, in this case, we would lose most of the information that is contained in the wave function. If the wave function is expressed in MO-based Slater-determinants, then one can use the CI-coefficients (c_i) as a basis of comparison. Due to the exponential formulation of CC wave functions, studied in our work in detail, contributions for all higher excited determinants are present even for CC truncated to single and double (SD) excitations. The expression of the full c_i is, however, numerically infeasible for the systems of our interest, as it would be as large as the FCI wave function, therefore it should also be truncated. Additionally, due to the internal normalization of the CC wave function, we can not determine the error caused by this

truncation, unless we evaluate all coefficients. Consequently, the comparison based on the CI coefficients will be restricted up to double excitations by projecting the wave functions to this subspace and then normalizing them,

$$|\Phi\rangle = \frac{\hat{P}|\Psi\rangle}{\|\hat{P}|\Psi\rangle\|_2} \tag{1}$$

where $|\Psi\rangle$ is the wave function expressed as the linear combination of all possible configurations. In the following, $|\Phi\rangle$ will denote the wave function projected on the basis of the reference determinant and the corresponding single and double excited configurations and then normalized, \hat{P} projects to the subspace of single and double excitations, and $\|\cdot\|_2$ stands for the usual norm of the wave function.

Reduced density matrices provide an alternative way to represent the quantum state. The one-particle reduced density matrix (1-RDM, γ) contains partial, compressed information about the wave function, and will also be used as an alternative basis of comparison. As CC is not a variational method, different formulations exist for the density matrices. In this work we used unrelaxed RDMs, i.e., response RDMs without orbital relaxaton effects.

As a distance metric, we will use the Euclidean norm of the differences of the normalized vector made of c coefficients (Ψ), or their projection c^{SD} up to doubles excitation (Φ), or the Hilbert–Schmidt norm of the differences of 1-body RDM matrices (γ). The distance from the reference wave function or RDM is denoted by d, while the basis of comparison is represented in the lower index.

$$d_{\Psi} = \|\Psi_{\text{CCSD}} - \Psi_{\text{DMRG}}\| \tag{2a}$$

$$d_{\Phi} = \|\Phi_{\text{CCSD}} - \Phi_{\text{DMRG}}\| \tag{2b}$$

$$d_{\gamma} = \|\gamma_{\text{CCSD}} - \gamma_{\text{DMRG}}\| \tag{2c}$$

We note that d_{Ψ} is only available for small systems, but d_{Φ} and d_{γ} can be evaluated efficiently for larger systems, too. In the following, if there is no subscript following d, we refer to the distance metric in general.

2.3. Active Space Selection. Although DMRG can handle active spaces close to a hundred orbitals, ^{49,52,54–58} the accessible number of orbitals is still lower than in CCSD, therefore the orbital space should be truncated.

A universally applicable black-box active space selection strategy is challenging to design. However, an automatized selection protocol based on single orbital entropies³⁰ introduced via the dynamically extended active space (DEAS) procedure, also utilized in a more general framework, ^{33,59} can offer a reasonable solution. In this procedure, an initial, low bond dimension DMRG is performed on the full valence space, and the active space is selected based on single-orbital entropies with an empirical preset cutoff relative to the highest observed entropy value.

In this study, we develop an alternative entropy-based selection. As a first step of the entire workflow, we perform a standard CCSD (or any other post-HF) calculation, which we later want to analyze and from which the Φ or γ can be easily extracted (light blue part of Figure 3). Recall that the single-orbital entropy³⁰ for orbital i is defined as

$$s_{i}(1) = -\sum_{\alpha} p_{i}^{\alpha} \ln p_{i}^{\alpha} \tag{3}$$

where p_i^α denotes the probability that orbital i is found in occupation state $\alpha \in \{0, \downarrow, \uparrow, \downarrow \uparrow\}$ in the many-body wave function. The p_i^α weights can be determined by summing the square of the CI coefficients of the corresponding determinants. We note that in practical CC calculations, we estimate the probabilities by restricting the CI expansion of the wave function up to double excitations. Alternatively, exact entropies could also be constructed from relevant entries of the 1- and 2-body reduced density matrices; $^{60-62}$ however, this requires solving the Λ equations besides the CC amplitude equations, which both have similar costs, while for the calculation of the energy the solution of the CC amplitude equations are sufficient.

By sorting the $s_i(1)$ values in descending order, the orbitals can be selected according to their chemical relevance, where orbitals with the highest entropies will form the active space.

However, the question remains how to choose the cutoff of $s_i(1)$ between the active and inactive orbitals. Here, instead of predefining a fixed $s_i(1)$ value or proportion, such as for example 10% in the AutoCAS program, ³³ we apply a different approach. Based on the sorted $s_i(1)$ values, we identify various subsets of orbitals by their importance, where active orbitals are distinguished from inactive ones by the rate of the change in the entropy profile. More precisely, orbitals labeled $\{1, ..., i\}$ in the descending entropy order define an active space in case of $s_{i-2}(1) - s_{i-1}(1) < s_{i-1}(1) - s_i(1)$ (i.e., the entropy difference between two adjacent orbitals is larger than previously).

In some way, we try to separate the static and dynamic correlation. In that sense, we are interested in how well the static correlation is described by the selected active space and not in the dynamic correlation mostly captured by the inactive orbitals. Once the possible active spaces are determined, starting from the smallest ones, we perform CCSD calculation for the selected active space, which results are marked by superscript AS. The obtained CCSD wave function (Φ^{AS}_{CCSD}) or RDM (γ^{AS}_{CCSD}) is compared to the corresponding projection of the full space CCSD wave function ($\Phi^{FS\to AS}_{CCSD}$). The corresponding distances are

$$d_{\Phi}^{\text{AS}} = \|\Phi_{\text{CCSD}}^{\text{AS}} - \Phi_{\text{CCSD}}^{\text{FS} \to \text{AS}}\| \tag{4a}$$

$$d_{\gamma}^{AS} = \|\gamma_{CCSD}^{AS} - \gamma_{CCSD}^{FS \to AS}\| \tag{4b}$$

Note that the full space Φ_{CCSD} and γ_{CCSD} are projected to the selected subspace, where only those configurations are kept, in which excitations are allowed for orbitals in the active space, hence, the "FS \rightarrow AS" in the upper index. The wave function and RDM are normalized to give 1 and the correct electron number, respectively.

By comparing wave functions of the full space CCSD and the one of the CCSD on active space, d^{AS} measures the error of active space selection. By definition, d^{AS} equals zero if all orbitals are active. Hence, the active space can be considered as converged once d^{AS} falls below a predefined threshold. If d^{AS} is larger than the desired threshold, we continue with including the next batch of orbitals in the active space proposed by the entropy profile until the defined criteria are satisfied. This selection approach ensures that we select a subspace that correctly represents the whole space. For small active spaces, it might happen that first d^{AS} increases (see later), therefore we apply a conservative approach, and d^{AS} have to be not only below a threshold, but have to be decreasing (be smaller than

the previous iteration). The whole active space selection is summarized by the light pink part of Figure 3.

The relation of the various wave functions is summarized in Figure 1, using BN at CCSD/cc-pVDZ level of theory as an

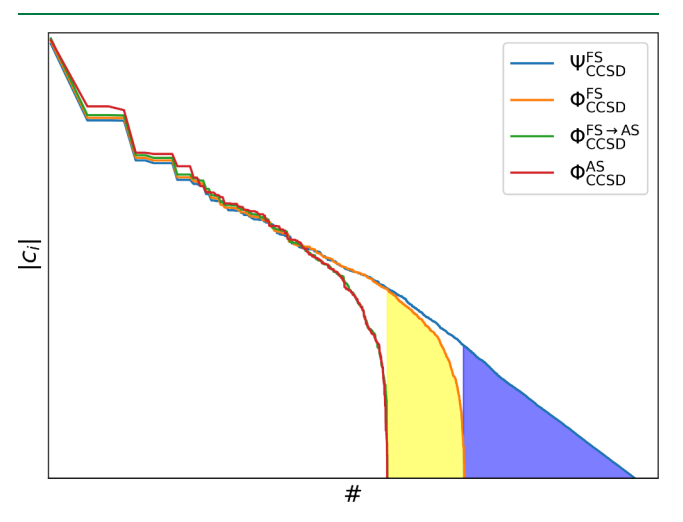


Figure 1. Schematic representation of the different normalized CCSD wave functions by plotting the corresponding CI coefficients for BN at the CCSD/cc-pVDZ level of theory and AS represents 14 orbitals. The blue shaded part represents the part of the wave function that is discarded by restricting up to double excitations. The yellow shaded part shows the determinants that are discarded due to the active space truncation.

example. First, we have $\Psi^{\rm FS}_{\rm CCSD}$ the full space CCSD wave function (accessible only for small systems). Though the number of cluster amplitudes are limited, due to the exponential ansatz, the CI coefficients are not. The evaluation of all coefficients is not practical, and it is limited up to double excitations; higher excitations, represented in blue shade, are ignored, and the error introduced with this truncation is unknown. $\Phi^{\rm FS}_{\rm CCSD}$ is the wave function with only single and double excitations, while $\Phi^{\rm FS \to AS}_{\rm CCSD}$ contains only the excitations that are in the active space. The error of this truncation is the yellow shaded area in the figure. Finally, we compare this wave function to $\Phi^{\rm AS}_{\rm CCSD}$, to get $d^{\rm AS}_{\Phi}$. We note that in the case of γ , there is only active space truncation and no exclusion of higher excitations.

2.4. Forming the Final Metric. Following the active space selection, a DMRG calculation is performed. This produces a third wave function, besides the existing active space and full space CCSD wave functions, which wave function we represent by its CI coefficients, c, or 1-RDM, γ . To ensure comparability, both three wave functions are vectors of the same active space and are normalized to one, and the electron number in 1-RDM's is also properly set.

Between the three wave functions, three distances can be defined, and one of them, d^{AS} , is already defined in eq 4. It is easy to see that as the size of the active space approaches full space the wave function of the two CCSD calculation become more and more similar,

$$\lim_{AS \to FS} \Phi^{AS}_{CCSD} = \Phi^{FS}_{CCSD} \tag{5a}$$

$$\lim_{AS \to FS} \gamma_{CCSD}^{AS} = \gamma_{CCSD}^{FS}$$
 (5b)

and, consequently,

$$\lim_{AS \to FS} d_{\Phi}^{AS} = 0 \tag{6a}$$

$$\lim_{AS \to FS} d_{\gamma}^{AS} = 0 \tag{6b}$$

It is important to note that the active space selection is based on the orbital entropies, meaning orbitals are included based on their importance in the wave function. The goal is to include all orbitals that are important to describe static correlations, while we aim to discard orbitals that are only contributing to the so-called dynamic correlation.

The other two are the distances from the DMRG solution,

$$d_{\Phi}^{a} = \|\Phi_{CCSD}^{FS \to AS} - \Phi_{DMRG}^{AS}\| \tag{7a}$$

$$d_{\gamma}^{\mathrm{a}} = \| \gamma_{\mathrm{CCSD}}^{\mathrm{FS} \to \mathrm{AS}} - \gamma_{\mathrm{DMRG}}^{\mathrm{AS}} \| \tag{7b}$$

and

$$d_{\Phi}^{b} = ||\Phi_{\text{CCSD}}^{\text{AS}} - \Phi_{\text{DMRG}}^{\text{AS}}|| \tag{8a}$$

$$d_{\gamma}^{b} = \|\gamma_{\text{CCSD}}^{\text{AS}} - \gamma_{\text{DMRG}}^{\text{AS}}\| \tag{8b}$$

Note again that in eq 7a the full space CCSD wave function has been projected to the active space and normalized to ensure comparability. At the full space limit, both of them are equal to d_{Φ} or d_{ν} value we are interested in

$$d_{\Phi} = \|\Phi_{\text{CCSD}}^{\text{FS}} - \Phi_{\text{DMRG}}^{\text{FS}}\| \tag{9a}$$

$$d_{\gamma} = \|\gamma_{\text{CCSD}}^{\text{FS}} - \gamma_{\text{DMRG}}^{\text{FS}}\| \tag{9b}$$

We can not choose from d^a and d^b which will be the better metric; therefore, both will be used. We note, however, that the triangle inequality holds for the 3 distances, and thus, the difference of d^a and d^b is bounded from above by d^{AS} ,

$$|d_{\Phi}^{a} - d_{\Phi}^{b}| < d_{\Phi}^{AS} \tag{10a}$$

$$|d_{\gamma}^{a} - d_{\gamma}^{b}| < d_{\gamma}^{AS} \tag{10b}$$

The relation of various wave functions, RDMs and d-s introduces in this section are summarized in Figure 2. Here we remark, as will be discussed in the following sections, that in practice the average value of d^a and d^b will be used denoted by d.

2.5. Possible Workflows. A general workflow is presented in Figure 3:

- 1. Perform CCSD calculation and obtain the basis of comparison (Φ^{FS}_{CCSD} or γ^{FS}_{CCSD}).
- 2. Perform orbital transformation for better active space selection (optional).

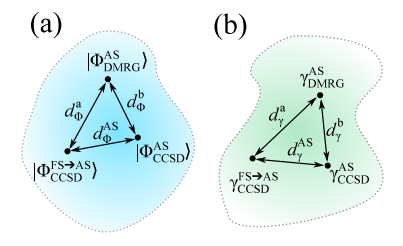


Figure 2. (a) Wave functions truncated to single and double excitations on the active space and the distances defined between them. (b) 1RDM-s on the active space and distances defined between them.

- 3. Determine orbital entropies based on c or 1- and 2-RDM
- 4. Select the most influential orbitals.
- 5. Perform CCSD on selected orbital space and obtain $\Phi^{\rm AS}_{\rm CCSD}$ or $\gamma^{\rm AS}_{\rm CCSD}$.
- 6. Check if d^{AS} is below threshold and smaller than the previous one $(d_{\text{previous}}^{AS})$, if yes, proceed, if not, repeat from step 4 by including more orbitals until true.
- 7. Perform orbital transformation for DMRG to aid better convergence (optional).
- 8. Perform DMRG and obtain $\Phi_{\rm DMRG}^{AS}$ or $\gamma_{\rm DMRG}^{AS}$
- 9. Detemine d^a and d^b .

Besides the DMRG accuracy and the d^{AS} threshold, we have to decide the basis of comparison also if we apply any orbital transformation. The threshold in d^{AS} controls the accuracy of the final result, while the size of the active space strongly influences the cost of the DMRG calculation. Using some kind of orbital transformation before the orbital selection can compress correlations and can result in smaller active spaces. However, we have to ensure the invariance of CCSD solution under orbital transformations. The transformation before DMRG, like localization, can lead to better convergence. Based on the options, we define 3 workflows to apply in this work:

- Workflow A: Use Φ as a basis of comparison, no orbital transformation before selection, split-localization before DMRG. The corresponding result is denoted by d_Φ.
- Workflow B: Use γ as a basis of comparison, no orbital transformation before selection, split-localization before DMRG. The corresponding result is denoted by d_γ.
- Workflow C: Use γ as a basis of comparison, use "split-natural" orbitals for selection, no additional transformation before DMRG. The corresponding result is denoted by $d_{\gamma,NO}$.

Workflow A is intended to apply when producing RDM-s would be too expensive. Workflow B is the same as A, but with γ instead of Φ , because it contains higher excitations from the wave function. Workflow C utilizes the fact that if the one-body RDM is at hand, then natural orbitals can be obtained. To keep the invariance of CCSD, the occupied and virtual orbitals should be transformed separately, also known as quasinatural orbitals. We expect that the usage of natural orbitals compresses the correlation and, consequently, less orbitals are needed than in workflow B. In this case, we do not use localized orbitals, because DMRG works well with natural orbitals too. 64,65

Importantly, even though the black-box computation of d requires two parameters (the d^{AS} threshold and DMRG truncation error) as input, we emphasize that the choice of these parameters is rather flexible. That is, if doubts arise about the reliability of d, for example surprisingly high d value (over 0.5) or significantly higher energy with DMRG than CCSD for the same active space, more than 0.01 E_h , a more accurate d can be computed at a larger active space and/or a lower truncation error.

Finally, we note that in the workflow both CCSD and DMRG can be substituted to any other method from which CI coefficients or the RDM can be extracted to estimate the distance between the wave functions of two methods.

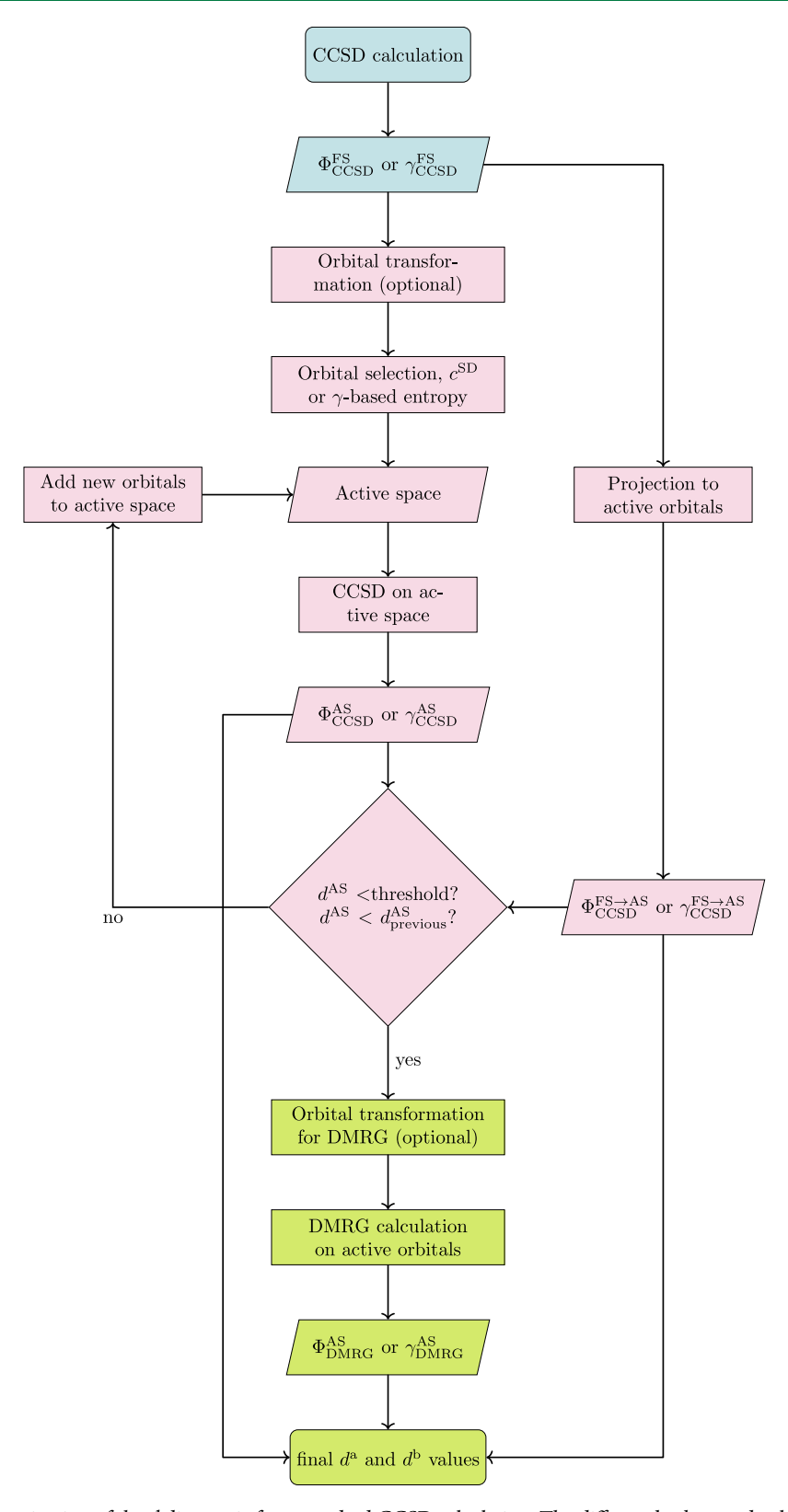


Figure 3. Flowchart of determination of the d diagnostic for a standard CCSD calculation. The different background coloring refers to the different steps, i.e., light blue: original CCSD calculation; light red: active space selection; light green: DMRG calculation and final d determination.

3. COMPUTATIONAL DETAILS

In this section, we present computational details. Geometries for the W4–17 data set have been taken from the Supporting Information of ref 66, for the 3d-MLBE20 data set from ref 67. Furthermore, nine 3d and nine 4d transition metal species

were studied from the work of Bradley et al. 68 using geometries from refs 69–75. These species will simply be termed 3d-TM9 and 4d-TM9.

As an additional challenge, we collected additional 3d and 4d species from the works of Jiang et al. 76 and Wang et al. 76

which are claimed to be MR. Additionally, based on the work of Süß and co-workers⁷⁷, species have also been added from the database of Aoto et al.,⁷⁸ which have at least 2.5 kcal/mol correction to their bond dissociation energy with icMR-CCSD(T) compared to CCSD(T), along with the additional 12 systems studied by Süß et al. Geometries were optimized at B3LYP/cc-pVTZ level of theory, except for species from the database of Aoto et al.⁷⁸ This collection of systems will be labeled as TM-MR. The full list of studied systems can be found in detail in Table S1.

CCSD⁷⁹ and CCSD(T)⁸⁰ calculations were performed using cc-pVDZ^{81–83} basis set and frozen core approximation without density fitting with MRCC.⁸⁴ A slight modification was made to obtain the CI coefficients from MRCC. Integrals for the subsequent DMRG calculation were also produced with MRCC. For open-shell species, the ROHF formalism was used.

The occupied and virtual orbitals were localized by Multiwfn⁸⁵ applying the Pipek–Mezey localization scheme.⁸⁶

All DMRG calculations were carried out with the Budapest-DMRG⁸⁷ program package via the DBSS formalism, ⁴⁴ by setting the maximum truncation error, ϵ , to 10^{-5} . The minimum value for the bond dimension was set to $D_{\rm min}=256$ and the maximum value was limited by $D_{\rm max}=4096$. For large active spaces DMRG orbital ordering was also optimized by a combination of the Fiedler-vector and genetic algorithm based protocols⁸⁸ performing a series of low-cost DMRG calculations with fixed D=32, 64, and 128 bond dimension values.

The various multireference diagnostics were already discussed in the Introduction; therefore, instead of a detailed description of each metric used in this work, we summarized them in Table 1.

Finite-temperature DFT calculations were performed with the default settings of the ORCA (version 5.0.3.⁸⁹) program. All other DFT calculations (BLYP,^{37,38} B1LYP,³⁹ PBE,⁹⁰ PBE0⁹¹) were performed with MRCC.

The whole workflow is controlled by an in-house-developed Python code. Additional MR diagnostics were also evaluated by Python scripts processing DMRG and CCSD CI coefficients and DMRG and CCSD RDMs to obtain occupation numbers along with FT-DFT fractional occupation number, CCSD amplitudes, and necessary energies for energy-based diagnostics.

To better understand the practical relationship between the metrics, we determined the pairwise correlation coefficients between different data sets. The commonly used Pearson correlation (r), which lacks robustness and can reveal only linear correlations, is not the most suitable statistic to compare the metrics studied. Correspondingly, in our study Spearman (ρ) and Kendall rank correlations were used: (τ)

$$\rho = \frac{\operatorname{cov}(R[x][R[y])}{\rho_{R[x]}\rho_{R[y]}} \tag{11}$$

$$\tau = \frac{2}{n(n-1)} \sum_{i < j} \operatorname{sgn}(x_i - x_j) \operatorname{sgn}(y_i - y_j)$$
(12)

where R[x] and R[y] are the ranks of x and y variables, and n is the number data points. They are more reasonable statistics, which uses the ranking of the values and are more robust to outliers. Kendall correlation separates the various metrics even

better. In short, we will refer to these correlation coefficients as r, ρ , and τ , respectively.

4. RESULTS AND DISCUSSION

In order to keep the focus on the practical application of *d*, in this section only the main summary of the validation protocol is discussed, while details can be found in the SI.

The first approximation is the truncation of the Ψ wave function up to double excitations (Φ). The comparison of d_{Ψ} and d_{Φ} shows that d_{Φ} holds its descriptive power, although slightly lower than that of d_{Ψ} .

The next approximation is the use of DMRG instead of FCI as an FCI solver. By varying the truncation error we found that at least a truncation error of 10^{-5} is needed for reasonable results.

The third approximation is the use of a subspace instead of the whole orbital set. In that sense, we checked the convergence of d^{AS} , d^a , and d^b with respect to the active space size. In general, larger active space leads to lower d^{AS} , i.e., better quality. d^a and d^b converge smoothly to the full space d in most cases, but, it varies species by species which of them is more useful. However, we noticed that their average, labeled as \tilde{d} , has better convergence than d^a and d^b in every case; therefore, \tilde{d} will be used to estimate d. Another observation is that the NO-transformation can lead to smaller d-s by introducing a bias to the CCSD solution. These findings are valid for both the Φ - and γ -based protocols.

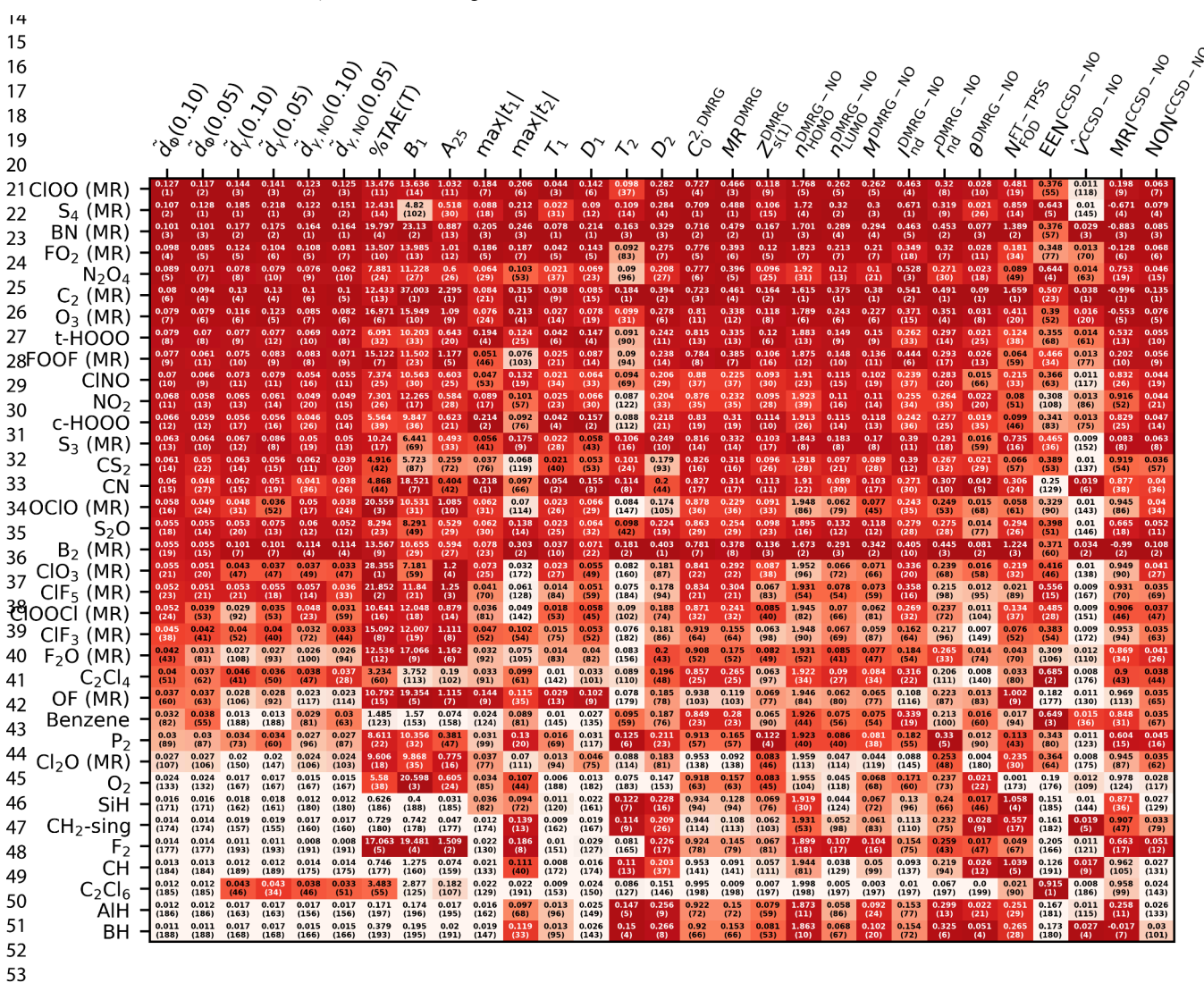
Based on these results, in the following, we will use two settings, a looser threshold of 0.1 and a tighter threshold of 0.05 for both d_{Φ}^{AS} and d_{γ}^{AS} . The corresponding results will be noted as $\tilde{d}_{\Phi}(0.1)$, $\tilde{d}_{\Phi}(0.05)$, $\tilde{d}_{\gamma}(0.1)$, and $\tilde{d}_{\gamma}(0.05)$, where the number in the paranthesis is the used d^{AS} threshold. An additional restriction is that the active space selection error should be lower than with the previous active space candidate to avoid a selection of active space before a local maximum.

4.1. Comparison of \tilde{d} and MR Diagnostics on the W4–17 Data Set. Before discussing the various \tilde{d} values, we take a look at the performance active space selection schemes. Using the looser 0.1 threshold obviously leads to smaller active spaces. As \tilde{d}_{γ} is usually higher than \tilde{d}_{Φ} , to reach the same threshold on the same set of canonical orbitals, RDM-based orbital selection leads to larger active spaces, 43% and 37% of the whole orbital space on average with a threshold of 0.05 for $d_{\gamma}^{\rm AS}$ and $d_{\Phi}^{\rm AS}$, respectively. However, as we have seen earlier, the usage of NO-transformation leads to less selected orbitals, 34% of the whole space on average if the threshold is 0.05. Note that these statistics are only valid for this data set; with larger basis sets we expect smaller ratios.

Instead of discussing the determined d values for the W4–17 data set alone, we will analyze them in relation to other existing MR diagnostics, which are listed in Table 1.

We think that both MR diagnostics and our \tilde{d} try to give guidance for the same problem; can we use a single reference method for a given system to obtain meaningful results? The difference is that MR diagnostics measure the MR character of the studied system, which is usually a metric of how different some property is from a reference, which usually is the ideal single reference wave function. In contrast, \tilde{d} takes a more practical approach and estimates the distance from the (approximate) FCI wave function. In line with their definition and philosophy, we expect a low correlation between MR diagnostics and \tilde{d} , but it is still worth comparing them since they deal with the same problem.

Table 2. \tilde{d} and Other Commonly Used MR Diagnostics for a Selected Subset of W4-17 Dataset



"It contains the W4-17-MR subset, marked with "MR", and additional species which has a \tilde{d} value in the top 15 or other metric which is in the highest 5 among the species of W4-17. The number in the cells shows the value of the corresponding metric, while in parentheses, the rank of this value among the species is presented. For better visibility, the rankings are also represented by the cell color, where a deeper red color means a higher ranking.

The quantum chemical method based on which we obtained the given diagnostic is presented in the corresponding superscript. For C_0^2 and MR we used the DMRG result instead of performing CASSCF. For metrics based on occupation numbers, CCSD- and DMRG-based RDMs were utilized to derive natural occupation numbers. Alternatively, fractional occupational numbers were also used from finite-temperature DFT. maxl t_1 l, maxl t_2 l, T_1 , D_1 , T_2 , and D_2 are determined from CCSD/cc-pVDZ calculations, %TAE(T) from CCSD(T)/cc-pVDZ, B_1 from BLYP/cc-pVDZ and B1LYP/cc-pVDZ, and A_{25} from PBE and PBE0 with cc-pVDZ, respectively.

The various MR diagnostic values for the MR subset are presented in Table 2. In cases where the definition allows multiple quantum chemical methods (e.g., metrics based on occupation numbers), we chose to show here the ones which are the closest to the definition in the original papers, while other versions can be found in the SI. For demonstrative purposes, we show herein all species where either \tilde{d} values are

in the top 15 or one of the other diagnostics listed have a top 5 value among the species of the W4–17 data set. The threshold when a species is labeled as a multireference is not always defined and is sometimes debatable. Although we label the members of the "MR" subset, as given in the W4–17 paper, 66 in Table 2 next to the molecular formula, we do not consider the W4–17-MR molecules as a specific group in our discussion. Instead, we rank the molecules of the W4–17 data set based on each investigated diagnostic value and use the ranking numbers as guidelines. This ranking is shown in the parentheses in Table 2 and is also visualized by the coloring.

The different \tilde{d} formulations consistently identify species with high \tilde{d} . The largest discrepancy is found for B₂, where $\tilde{d}_{\Phi}(0.05)$ gives 0.055, which can be considered a relatively high value among \tilde{d}_{Φ} -s, while $\tilde{d}_{\gamma}(0.05)$ and $\tilde{d}_{\gamma,\mathrm{NO}}(0.05)$ produce 0.101 and 0.114, respectively. Other notable differences are benzene with a relatively small \tilde{d}_{γ} (0.013) and C₂Cl₆ with a

4c(CCSD) 4a(DMRG) 4a(CCSD) 4b(CCSD) 4d(CCSD) 4b(DMRG)4d(DMRG)4(FT-TPSS) 1 $\tilde{d}_{\Phi}(0.10)$ $\tilde{d}_{\Phi}(0.05)$ $\tilde{d}_{\nu}(0.10)$ 1 $\tilde{d}_{v}(0.05)$ $\tilde{d}_{\gamma,\,NO}(0.10)$, _{NO}(0.05) %TAE(T) $\max |t_1|$ 3 $\max |t_2|$.320.32 0.22 0.24 0. 4a(CCSD) MRICCSD - NO NON^{CCSD - NO} MR CCSD IccsD - NO 4b(CCSD) 35 0.05 0 36 0.06 0 06 0.01 EENCCSD - NO $Z_{s(1)}^{CCSD-CI}$ 0.230.23 0.11 0.12 0 SD – RDM 4c(CCSD) 0.4 0.4 0.29 0.3 0 r_{nd} - NO .260.26 0.16 0.17 0. 4d(CCSD) 140.14 0.15 -0.060. VCCSD - NO n_{HOMO} - NO 4a(DMRG) 0.37 0.42 0.41 0 340.34 0.22 0.24 0. MRI^{DMRG - NO} NONDMRG - NO $C_0^{2, DMRG}$ MR DMRG 32 0.29 4b(DMRG) 2 0.3 NDMRG - NO NDMRG - NO 4c(DMRG) 4d(DMRG) 41 0.14 0 MRIFT - TPSS NONFT - TPSS Ind - TPSS 4(FT-TPSS) NFT - TPSS EENFT - TPSS 41 0.15 0

Table 3. Pairwise Spearman Rank Correlation Matrix of d and Other MR Diagnostics for the W4-17 Dataseta

^aThe more intense red hue represents a higher correlation. The left and lower labels show the metrics, while the right and upper labels show the corresponding groups.

relatively high \tilde{d}_{γ} (0.043) compared to \tilde{d}_{Φ} values (0.038 and 0.012) and rankings.

 $\tilde{a}_{\Phi}(0.10)$ $\tilde{a}_{\Phi}(0.05)$ $\tilde{a}_{\gamma}(0.10)$ $\tilde{a}_{\gamma}(0.05)$ $\tilde{a}_{\gamma}(0.05)$ $\tilde{a}_{\gamma}(0.05)$

In general, the looser and tighter thresholds for active space produce similar results, but the different formulations differ considerably. \tilde{d}_{Φ} -s are smaller than \tilde{d}_{ν} due to the fact that c coefficients are used up to double excitations. Another thing that was noticed earlier was that NO-transformation also leads to smaller d values, even though we expect similar results. A more detailed statistical analysis will be discussed later.

Considering the rest of the metrics, there are numerous discrepancies in the studied species. From ClOO to B₂ (upper half of the table) most diagnostics and d have high values, but $\max |t_2|$, T_2 , EEN, and V disagree with them notably. Regarding the W4-17 classification, which is based on the %TAE(T)

diagnostics, N2O4, t-HOOO, c-HOOO, NO2, S2O, CS2, and CN are species with a notable \tilde{d} (higher than 0.05) but are not part of the MR subset. However, OClO, ClOOCl, ClF₃, F₂O, OF, and Cl₂O all have \tilde{d} (0.05)-s less than 0.05, although they are part of the W4-17-MR subset. Hydrides are interesting cases because \tilde{d} and energy-based metrics show low values, but T_2 , D_2 , n_{HOMO} , M, I_{nd} , r_{nd} , θ , FOD, \hat{V} , and MRI show significant MR character. For energy-based diagnostics, Cl_2O , O_2 , and F_2 seem to be problematic cases.

To better understand the practical relationship between the metrics, we determined the pairwise correlation coefficients (r, r) ρ_1 and τ). Table 3 shows the Spearman rank correlation matrix, while the other two (r, τ) can be found in SI.

First, we look at the correlation between the \tilde{d} metrics. The correlation between the same metrics with different active space thresholds is close to 1 (r=0.97-0.98, $\rho=0.97-0.99$, $\tau=0.87-0.94$). However, between the three different types of \tilde{d} metrics, there is a lower but still strong correlation. $\tilde{d}_{\Phi}-\tilde{d}_{\gamma}$ have r=0.86-0.91, $\rho=0.80-0.82$, $\tau=0.63-0.66$; $\tilde{d}_{\Phi}-\tilde{d}_{\gamma,\mathrm{NO}}$ have r=0.86-0.90, $\rho=0.85-0.87$, $\tau=0.68-0.70$; and $\tilde{d}_{\gamma}-d_{\gamma,\mathrm{NO}}$ have r=0.92-0.96, $\rho=0.86$, $\tau=0.69-70$.

Based on these statistics, the metrics can be categorized into a few groups (see Table 4). The different \tilde{d} metrics are in their

Table 4. Groupings of MR Diagnostics Based on Pearson, Spearman, and Kendall τ Correlations of Each Metrics Result on the Species of the W4–17 Dataset

1	2	3	4a	4b	4c	4d
$ ilde{d}_{\Phi}$ $ ilde{d}_{\gamma}$ $ ilde{d}_{\gamma,\mathrm{NO}}$	%TAE(T)	$\max t_1 $	$\max t_2 $	C_0^2	$Z_{\mathrm{s}(1)}$	T_2
$ ilde{d}_{\gamma}$	B_1	T_1	D_2	MR	$r_{ m nd}$	θ
$ ilde{d}_{\gamma,\mathrm{NO}}$	A_{25}	D_1	n_{HOMO}	$I_{ m nd}$		\hat{V}
			$n_{ m LUMO}$	$N_{ m FOD}$		
			M	EEN		
			NON			
			MRI			

own category (group 1) and do not correlate with any other metrics, which is understandable because they are totally different from the others and try to answer a different question. Energy-based descriptors (%TAE(T), B_1 , A_{25}) have their own group (group 2). This is not surprising because all of them use total atomization energies. The metrics derived from single amplitudes (maxl t_1 l, T_1 , and D_1) are also separated from the other diagnostics (group 3), which mostly measure orbital relaxation effects. However, for other multireference diagnostics the main distinguishing property is not the formulation but the source of the data, i.e., occupation number and entropy-based diagnostics are grouped by if they derived from CCSD, DMRG, or FT-DFT. Within these groups, the metrics can be further divided.

Group 4a contains the simple occupation number-based diagnostics ($n_{\rm HOMO}$, $n_{\rm LUMO}$, M, NON), and surprisingly MRI, which is a complex transformation of them. Also, NON is basically the spin—orbital version of $n_{\rm LUMO}$. In group 4b we can see C_0^2 and MR are closely related, because C_0^2 is the largest contributor of MR. EEN and $N_{\rm FOD}$ are also defined in a way that they are identical, only $N_{\rm FOD}$ is half of EEN. $I_{\rm nd}$ also has a similar form to MR ($\sum_{\sigma,i} n_i^{\sigma}(1-n_i^{\sigma}) = \sum_{\sigma,i} n_i^{\sigma}-n_i^{\sigma^2} \sim \sum_i |c_i|^2 -|c_i|^4$). θ and \hat{V} in group 4d also have a similar philosophy by taking the difference of occupation numbers from the ideal and scaling with the number of electrons.

Notice that metrics from double amplitudes can also be sorted in this grouping with other diagnostics derived from CCSD natural orbital occupations. Looking at the off-diagonal elements, we can see that the subgroups of group 4 are fairly correlated for diagnostics derived from DMRG and FT-DFT (except for MRI^{FT-TPSS}), while in the case of CCSD, the subgroups are much more separated, especially group 4b. For DMRG, the reason might be that approaching FCI the differences between the various MR definitions are getting smaller. In the case of FT-TPSS data, we can observe that the default settings produce occupation numbers that do not differ from the occupation of the reference state, leading to small separation for SR species and large deviation from other metrics.

Group 1 has some noticeable correlation only with group 3 (r=0.53-0.77, $\rho=0.61-0.82$ $\tau=0.44-0.63$), and \tilde{d}_{Φ} has noticable correlation with DMRG-based groups 4a and 4b (r=0.67-0.84, $\rho=0.56-0.74$ $\tau=0.40-0.54$). These are not that high; therefore, \tilde{d} cannot be estimated using other existing MR diagnostics. Another connection can be observed between the members of the CCSD and the DMRG-based subgroup 4a (r=0.68-0.95, $\rho=0.73-0.95$, $\tau=0.55-0.81$).

Earlier comparisons found conclusions similar to those we did. Fogueri et al.⁸ showed that various A_{λ} and %TAE formulations correlate well with each other, and C_0^2 and Mform another group. Duan and co-workers⁶ studied 15 MR diagnostics and also concluded that the source of the data for the diagnostics is an important factor. They could also distinguish energy-based descriptors from other metrics, such that T_1 and D_1 behave similarly, and D_2 correlates moderately well with other occupation-based diagnostics. Most recently, Martin et al.40 studied the correlation between various MR diagnostics and derived TAEx. They determined four clusters: (1) T_1 , D_1 , max t_1 ; (2a) r_{nd} , \overline{I}_{nd} (divided by the number of electrons, not 2, leading to the same expression as \hat{V}); (2b) M, D_2 , max $|t_2|$; (3) energy-based diagnostics. These groupings are in line with our findings. Xu et al.⁹³ showed a connection between $\overline{I}_{\rm nd}$ and C_0 , and also between D_2 and maximum of $n_i^{\sigma}(1-n_i^{\sigma})$ values, labeled as $I_{\rm nd}^{\rm max}$. We already grouped the unscaled I_{nd} and C_0^2 together; however, the size effects are less prominent in the used data set. In a more recent work⁹⁴ they compared several MR diagnostics, and they determined five groups of correlation measures. From these, the dynamic natural orbital occupation (NOO)-based correlation measure $(\overline{I_{\mathrm{D}}})$ is not a good MR diagnostic, while average NOO-based nondynamic correlation measures ($\overline{I_{
m nd}}$ and $\%I_{\rm nd} = \overline{I_{\rm nd}}/(\overline{I_{\rm nd}} + \overline{I_{\rm d}}) \times 100$) could correspond to our 4b group. Maximal nondynamic correlation measures that include $I_{
m nd}^{
m max}$, n_H , n_L (maximum and minimum occupancy of occupied and virtual natural spinorbitals), $-\log(I)$ (connected to MRI, defined in Table 1), M, and D_2 are similar to our group 4a. D_1 and T_1 are in t_1 -based correlation measures, as in our group 3, and energy-based correlation measures correspond to our

Recently, Stanton and his co-workers presented Density Asymmetry Diagnostic (DAD), 95 which measures the antisymmetry of the 1-RDM of a CC calculaton. In our used code packages (MRCC) such a quantity is not accessible, and only the real symmetrized part of the 1-RDM is returned. Therefore, we did not determine DAD for the studied species but compared our numbers on the W4–11 subset that they used. In this subset, DAD belongs to group 3.

Based on these findings, we can conclude that none of the existing MR diagnostics provides information similar to that of any formulation of \tilde{d} . However, this is not surprising if we consider that our new metric measures a different property, estimating the distance from the exact solution, while the rest of the MR diagnostics measure the deviation from the ideal single reference solution. Following this line of thought, we are not classifying systems as MR or SR based on \tilde{d} , but rather evaluate the suitability of the method used, here CCSD. \tilde{d} increases with the size of the system, and based on the comparison of alkanes and halogenated alkanes (Table S5.) found that this scaling is proportional to the number of non-H or heavy atoms (N_{heavy}) . Using this scaling, if \tilde{d}_{γ} is below $0.03536 \times \sqrt{N_{\text{heavy}}}$, we consider that the used method is

Table 5. \tilde{d} Values for Species of W4-17 with $\tilde{d}_{\nu}(0.05)$ over 0.075 for the CCSD/cc-pVDZ Calculations

	CCSD/cc-pVDZ			CCSD/cc-pVTZ			CCSDT/cc-pVDZ		
species	$\tilde{d}_{\Phi}(0.05)$	$\tilde{d}_{\gamma}(0.05)$	$\tilde{d}_{\gamma,\mathrm{NO}}(0.05)$	$\tilde{d}_{\Phi}(0.05)$	$\tilde{d}_{\gamma}(0.05)$	$\tilde{d}_{\gamma,\mathrm{NO}}(0.05)$	$\tilde{d}_{\Phi}(0.05)$	$\tilde{d}_{\gamma}(0.05)$	$\tilde{d}_{\gamma,\mathrm{NO}}(0.05)$
B_2	0.055	0.101	0.114	0.053	0.121	0.125	0.013	0.023	0.033
BN	0.101	0.175	0.164	0.106	0.195	0.170	0.025	0.028	0.029
C_2	0.094	0.130	0.100	0.096	0.165	0.149	0.021	0.026	0.026
Clno	0.066	0.079	0.055	0.065	0.072	0.057	0.028	0.027	0.031
Cloo	0.117	0.141	0.125	0.111	0.140	0.130	0.027	0.026	0.022
FO_2	0.085	0.104	0.081	0.084	0.103	0.091	0.028	0.028	0.025
FOOF	0.061	0.083	0.071	0.067	0.095	0.066	0.029	0.036	0.029
N_2O_4	0.071	0.079	0.062	0.071	0.081 ^a	0.062	0.034	0.038	0.047
O_3	0.079	0.123	0.082	0.082	0.138	0.083	0.026	0.031	0.028
S_2O	0.055	0.075	0.052	0.062	0.064	0.049	0.026	0.032	0.026
S_3	0.064	0.086	0.050	0.075	0.105	0.049	0.022	0.036	0.027
S_4	0.128	0.218	0.151	0.122^{b}	0.221 ^a	0.158	0.032	0.059	0.059
t-HOOO	0.070	0.077	0.072	0.071	0.076	0.070	0.022	0.028	0.026
${}^{a} ilde{d}_{\gamma}(0.07). {}^{b} ilde{d}_{\Phi}(0.07).$									

highly reliable, while if \tilde{d} is over 0.07071 $\times \sqrt{N_{\text{heavy}}}$, then the used method is not reliable, based on the numerical results of the W4–17 data set. Between the two thresholds, the used method is moderately reliable. The respective thresholds for \tilde{d}_{Φ} are $0.03 \times \sqrt{N_{\text{heavy}}}$ and $0.06 \times \sqrt{N_{\text{heavy}}}$. We note that these thresholds are arbitrary, as most of them do not have strict criteria because we do not have another reference on which we can decide the thresholds. Based on these limits according to $\tilde{d}_{\gamma}(0.05)$, the calculations of BN, S₄, C₂, ClOO, B₂, and O₃ are problematic, and FO₂, S₃, ClNO, t-HOOO, S₂O, FOOF, CN, and NO₂ are moderately difficult for CCSD.

We also note here the differences between the different \tilde{d} -s. Generally \tilde{d}_{Φ} -s are smaller than \tilde{d}_{γ} but both have the predictive power to estimate the difference from the FCI. $\tilde{d}_{\gamma, \text{NO}}$ should lead to a similar value as \tilde{d}_{γ} but with fewer selected orbitals; however, in some cases, NO-transformation introduces a bias to the original CCSD solution, leading to a more similar DMRG solution and smaller $\tilde{d}_{\gamma, \text{NO}}$.

We close this section by emphasizing that the \tilde{d} diagnostic values are clearly attached to the studied calculation. To highlight this important feature, we determined the same d(0.05) metrics but with CCSD/cc-pVTZ and CCSDT/ccpVDZ calculation for systems which have $\tilde{d}_{\nu}(0.05)$ over 0.075 (Table 5) to see the effect of the basis set and method. As expected, really similar values have been obtained with the larger cc-pVTZ basis set, as with the smaller cc-pVDZ. As for the method, it is clear that eventhough CCSD might be inappropriate in some cases, higher-level methods, like CCSDT, have no problem with the species in question. This is demonstrated by the low (<0.05) values of d(0.05) for all species and formulations, except S_4 which have a $d_{\nu}(0.05) =$ 0.059 with CCSDT, which is still significantly lower than 0.218 for CCSD. This finding also proves the applicability of highaccuracy thermochemical models like Wn, HEAT, cccA, etc. for the W4-17 data set.

4.2. Application of the *d* Metric to Transition Metal Species. The multireference character among the transition metal species is much more common due to the several low-lying states. In these cases, choosing a reliably accurate, yet numerically affordable, approach can be more problematic. For main group species, the single reference methods usually give correct results; even sub-kJ/mol accuracy is achievable. However, the usage of multireference methods is more

complicated, and there is no gold standard such as CCSD(T) for single reference systems yet.

In such challenging situations, the usage of \tilde{d} metrics can be even more helpful to decide if a single reference method is applicable to a transition metal species in question. We demonstrate the concept by applying the \tilde{d} metric for the 3dMLBE data set⁶⁷ and for species studied with s-ccCA recently⁶⁸ labeled as 3d-TM9 and 4d-TM9 for 3d and 4d transition metal species, respectively. For comparison, results based on the \tilde{d} analysis are presented in Figure 4. The 3d-MLBE20 data set is divided into two subsets where 7 species are considered as single reference and 13 species are considered MR. In case of the 3d-MLBE20-SR subset \tilde{d} -s are fairly low, mostly below 0.05, only CuCl and ZnS show moderately high values, $\tilde{d}_{\gamma}(0.05)$ is 0.066 and 0.059, respectively.

From the 3d-MLBE20-MR subset, VH, VCl, CrH, FeH, CoCl, and CuH all have $\tilde{d}(0.05)$ -s below the corresponding threshold, showing that CCSD is adequate for studying these systems, although it is in the MR subset. TiCl and CoH have exceptionally high $\tilde{d}_{\gamma}(0.05)$ values (0.427 and 0.305), but in the case of TiCl $\tilde{d}_{\gamma,\mathrm{NO}}(0.05)$ it completely disagrees (0.045). This is the most spectacular case where the NO-transformation causes such a deviation. VO, CrO, and ZnO also have relatively high \tilde{d} -s, mostly over 0.1.

Looking at 3d-TM9 and 4d-TM9, in ref 68, the multireference character was classified according to the criteria of $T_1 > 0.05/0.045$, $D_1 > 0.15/0.12$, and %TAE(T) > 10%/10% for 3d and 4d species, respectively. Based on this metric, seven 3d species (ScB, ScC, ScS, TiB, VB, VC, and VS) and zero 4d species are considered to have multireference character. However, every \tilde{d} is greater than 0.05, suggesting that at most only moderately adequate to use CCSD for them. 3d-TM9 species are especially challenging; there are only two species with $\tilde{d}_{\gamma}(0.05)$ below 0.1, ScB (0.076) and ScC (0.099). 4d-TM9 species are mostly between 0.05 and 0.10, although clasified as a single reference, NbC even shows a $\tilde{d}_{\Phi}(0.05)$ of 0.148.

As an additional challenge, we determined $\tilde{d}_{\Phi}(0.10)$ and $\tilde{d}_{\gamma}(0.10)$ values for species labeled as TM-MR, selected from refs 7, 76, and 77, which are claimed to be MR systems. Based on the size-dependent thresholds determined in the previous section, FeCN, YC₂, and RuC have low $\tilde{d}(0.1)$ values, suggesting that CCSD is adequate for them. For ScO, TiB,

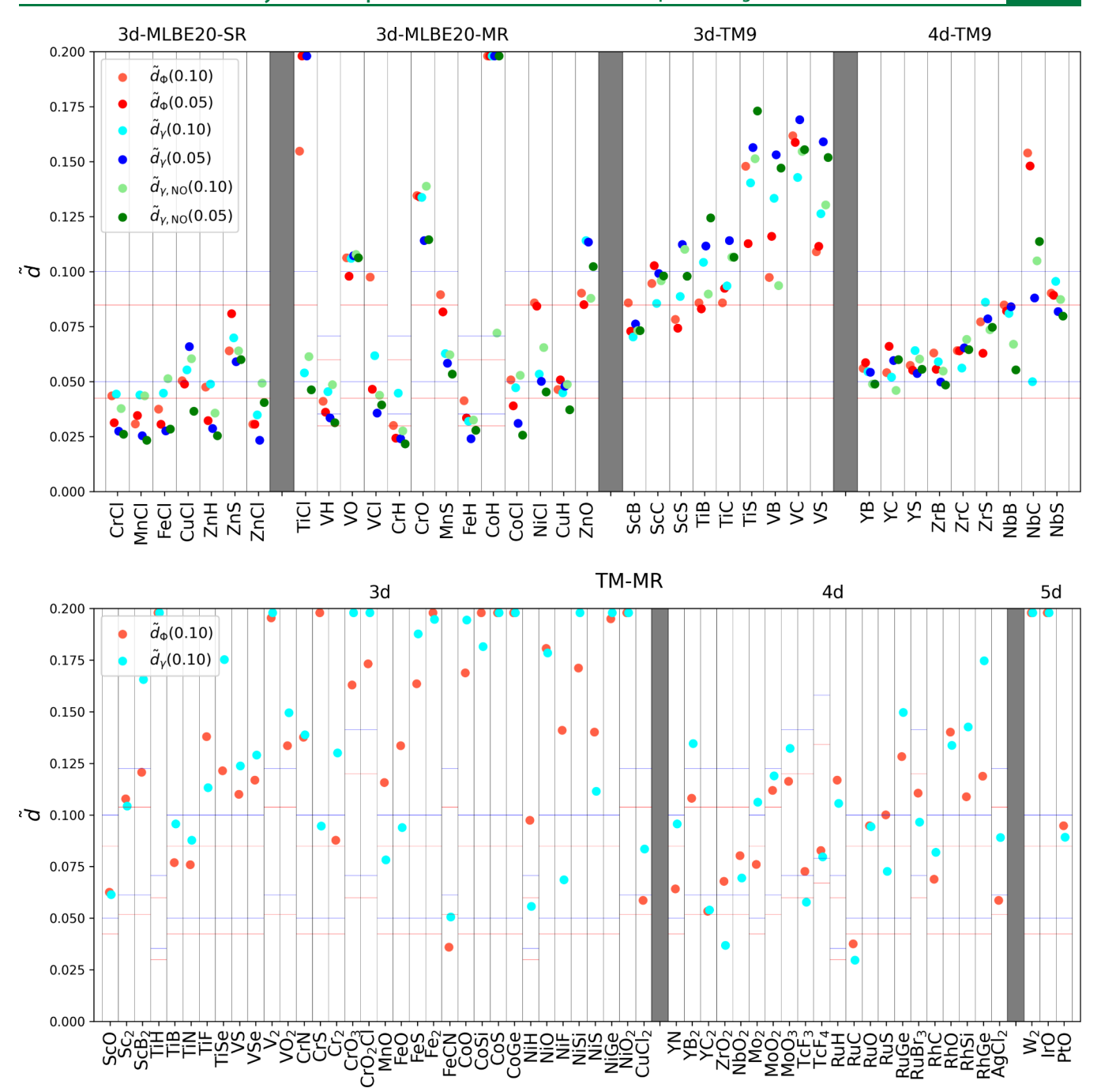


Figure 4. \tilde{d} values for the TM species studied in this work. Horizontal red and blue lines represent the lower and upper thresholds for the \tilde{d}_{Φ} and \tilde{d}_{γ} values, respectively.

TiN, CuCl_2 , YN, ZrO_2 , NbO₂, MoO₃, TcF₃, TcF₄, RuBr₃, RhC, and AgCl₂, both \tilde{d} variants are between their respective thresholds, meaning that one should be careful using CCSD. Some systems have differing $\tilde{d}_{\Phi}(0.10)$ and $\tilde{d}_{\gamma}(0.10)$ values, placing them on different sides of the higher threshold. These species are CrS, Cr₂, MnO, FeO, NiH, NiF, Mo₂, MoO₂, RuO, RuS, and PtO. The rest of the species are problematic for CCSD, especially TiH, V₂, CrO₃, CrO₂Cl, Fe₂, CoS, CoGe, CoSi, NiSi, NiGe, NiO₂, W₂, and IrO for which one of the $\tilde{d}(0.01)$ -s values is over 0.2.

Note that, in line with the previous findings, ^{96–98} our results show that even if a system is regarded as multireference by

some criteria, it may be handled with single reference CC to provide reliable data.

Regarding the composition of active spaces, we found high variance. For simpler systems, the occupied d and a few virtual d orbitals with low principal numbers of a given TM and some occupied and virtual s and p orbitals from the ligand is enough based on convergence, but the proper description of more correlated systems asks for orbitals with even higher principal numbers (4d, 5d, etc.) both for the TM and non-TM atoms.

Before concluding this section, we want to highlight another application of the framework presented in this paper. With DMRG the different excited states can be easily determined, which is useful especially in the case of transition metal species

to determine the correct ground state which can be problematic to find. Usually within this framework, such problems are highlighted with extremely high \tilde{d} values, over 1. In such cases, asking for more eigenvalues from the DMRG calculation and looking at the most dominant determinants can help identify the correct ground state. In this work, we found that the ground state of FeH is not $^4\Delta$, but $^6\Delta$, of CoCl not $^3\Phi$, but $^5\Delta$, YC is not $^4\Pi$, but $^4\Sigma$, and YC₂ is not 2B_2 , but 2A_1 . Note that this is only true for cc-pVDZ basis set; it is possible that the order of these closely lying states are changing with increased basis sets. However, such cases require a more careful approach and study of the possible occupations.

5. CONCLUSION

In this work, we present a new strategy to determine the quality of post-HF wave functions. Instead of trying to measure the deviation from the ideal single reference picture, as many multireference diagnostics do, we measure the difference from an approximate FCI solution. Here, we focus on the CCSD to demonstrate the applicability of the workflow. To this end, a subset of orbitals is chosen based on the CCSD solution, and a DMRG calculation is performed on them. Then the wave functions up to double excitations, Φ or 1-body RDM-s, γ , are compared from DMRG and CCSD to give a single metric labeled as \tilde{d}_{Φ} and \tilde{d}_{γ} .

We also introduced an orbital selection procedure that ensures that the selected subspace correctly represents the entire space. During this procedure, the orbitals are ranked by their relative importance derived from the CCSD solution, and on the selected subspace, another CCSD is performed, and the Φ -s or γ -s are compared to the original CCSD solution. The subspace is increased until the two CCSD solutions are similar enough. This method enables us to tune the accuracy of the \tilde{d} . The usage of natural orbitals from the CCSD before orbital selection was also tested, assuming it helps to select smaller subspaces.

Three different workflows were tested on the W4–17 data set and compared with other popular multireference diagnostics. The three flavors of \tilde{d} correlate well with each other $(\tilde{d}_{\Phi}, \tilde{d}_{\gamma}, \text{ and } \tilde{d}_{\gamma, \text{NO}})$. \tilde{d}_{Φ} is usually smaller than \tilde{d}_{γ} ; therefore, with the same active space selection threshold, γ -based selections are somewhat larger. However, NO-transformation produces smaller active spaces, but also introduces a bias to the CCSD solution that leads to smaller $\tilde{d}_{\gamma, \text{NO}}$ than \tilde{d}_{γ} .

None of the metrics were found to correlate well with \tilde{d} -s. MR diagnostics were also grouped by their performance and found that the source of the data is as important as the formulation of the MR diagnostic itself. The following groups were determined, which are in line with previous findings: group 2: %TAE(T), B_1 , A_{25} ; group 3: $\max |t_1|$, T_1 , D_1 ; group 4a: n_{HOMO} , n_{LUMO} , M, MRI, NON, $\max |t_2|$, D_2 ; group 4b: C_0^2 , MR, I_{nd} , N_{FOD} , EEN; group 4c: $Z_{\text{s}(1)}$, r_{nd} ; group 4d: θ , \hat{V} T_2 .

The proposed approach was also tested on transition metal species. VH, VCl, CrH, FeH, CoCl, and CuH have \tilde{d} -s below 0.05 with CCSD, showing that it is an adequate method to use on them, despite being in the MR subset. All 3d-TM9 and 4d-TM9 species have $\tilde{d}_{\gamma}(0.05)$ -s over 0.05 highlighting, which means these are at least moderately challenging. Additionally, 3d species are above 0.1, with the exception of ScB; therefore, CCSD is not recommended to study them. For a selection of MR transition metal species, we found that the calculation of FeCN, YC₂, and RuC are not problematic, and ScO, TiB, TiN,

CuCl₂, YN, ZrO₂, NbO₂, MoO₃, TcF₃, TcF₄, RuBr₃, RhC, and AgCl₂ are only moderately difficult for CCSD.

With regard to FeH, CoCl, YC, and YC₂ molecules, we predicted ground states different from those of the literature findings; nevertheless, these results are inconclusive because of the potential basis set sensitivity of the problems. However, our results demonstrate that the proposed procedure is also capable of finding the correct ground state, which is not always straightforward in transition-metal chemistry.

Based on the results, we find that in the case where \tilde{d}_{γ} (\tilde{d}_{Φ}) is below 0.03536 × $\sqrt{N_{\text{heavy}}}$ (0.03 × $\sqrt{N_{\text{heavy}}}$), the method used is a dequate, while for $\tilde{d}_{\gamma} > 0.07071 \times \sqrt{N_{\text{heavy}}}$ ($\tilde{d}_{\Phi} > 0.06 \times \sqrt{N_{\text{heavy}}}$) the used method is not reliable and other approaches are suggested to study the system in question. In the intermediate region of \tilde{d} , one should be cautious with the derived results. It must be noted that these limits are not strict, just recommendations based on the results in this work.

The approach presented here can be applied to test the quality of any wave function method where CI coefficients or RDMs can be extracted and a proper active space can be selected. In the matter of high-level reference methods, DMRG can be substituted for any reference-free method that is capable of providing an approximate FCI solution for large enough active spaces. This way the approach has the potential to become a quality assurance tool for wave function based methods.

ASSOCIATED CONTENT

Supporting Information

The Supporting Information is available free of charge at https://pubs.acs.org/doi/10.1021/acs.jctc.5c00750.

Results for W4–17 and transition metal species, MR diagnostics for W4–17, and Pearson, Spearman, Kendall correlation statistics between the diagnostics (XLSX) Geometries of the studied species (ZIP)

Validation of the introduced approximations and additional figures and tables (PDF)

AUTHOR INFORMATION

Corresponding Author

Adám Ganyecz – Strongly Correlated Systems "Lendület" Research Group, Wigner Research Centre for Physics, H-1525 Budapest, Hungary; orcid.org/0000-0002-8828-0283; Email: ganyecz.adam@wigner.hun-ren.hu

Authors

Zsolt Benedek – Department of Physics of Complex Systems, Eötvös Loránd University, H-1053 Budapest, Hungary; MTA–ELTE Lendület "Momentum" NewQubit Research Group, Pázmány Péter, 1117 Budapest, Hungary

Klára Petrov – Department of Physical Chemistry and Materials Science, Faculty of Chemical Technology and Biotechnology, Budapest University of Technology and Economics, H-1111 Budapest, Hungary

Gergely Barcza – Strongly Correlated Systems "Lendület" Research Group, Wigner Research Centre for Physics, H-1525 Budapest, Hungary

András Olasz – Strongly Correlated Systems "Lendület" Research Group, Wigner Research Centre for Physics, H-1525

- Budapest, Hungary; Furukawa Electric Institute of Technology Ltd., H-1158 Budapest, Hungary
- Miklós A. Werner Strongly Correlated Systems "Lendület" Research Group, Wigner Research Centre for Physics, H-1525 Budapest, Hungary
- Ors Legeza Strongly Correlated Systems "Lendület" Research Group, Wigner Research Centre for Physics, H-1525 Budapest, Hungary; Institute for Advanced Study, Technical University of Munich, 85748 Garching, Germany; Parmenides Stiftung, 82343 Pöcking, Germany; Dynaflex Ltd., H-1028 Budapest, Hungary; Orcid.org/0000-0002-9746-5802

Complete contact information is available at: https://pubs.acs.org/10.1021/acs.jctc.5c00750

Notes

The authors declare no competing financial interest.

ACKNOWLEDGMENTS

This work was supported by the Ministry of Innovation and Technology and the National Research, Development and Innovation Office of Hungary (NKFIH) within the National Quantum Technology Program (Grant No. 2022-2.1.1- NL-2022-00004) and Grant Nos. K134983, TKP2021-NVA-04, PD-146265, FK-135496. Ö.L. acknowledges support of the Hans Fischer Senior Fellowship programme funded by the Technical University of Munich - Institute for Advanced Study, and of the Center for Scalable and Predictive methods for Excitation and Correlated phenomena (SPEC), funded as part of the Computational Chemical Sciences Program FWP 70942 by the U.S. Department of Energy (DOE), Office of Science, Office of Basic Energy Sciences, Division of Chemical Sciences, Geosciences, and Biosciences at Pacific Northwest National Laboratory. Z.B. acknowledges the financial support of the János Bolyai Research Fellowship of the Hungarian Academy of Sciences. M.A.W. has also been supported by the Janos Bolyai Research Scholarship of the Hungarian Academy of Sciences. We also acknowledge KIFU for awarding us access to computational resources based in Hungary.

REFERENCES

- (1) Mok, D. K.; Neumann, R.; Handy, N. C. Dynamical and nondynamical correlation. *J. Phys. Chem.* **1996**, *100*, 6225–6230.
- (2) Scuseria, G. E.; Tsuchimochi, T. Constrained-pairing mean-field theory. II. Exact treatment of dissociations to nondegenerate orbitals. *J. Chem. Phys.* **2009**, *131*, na.
- (3) Hollett, J. W.; Gill, P. M. The two faces of static correlation. *J. Chem. Phys.* **2011**, 134, na.
- (4) Margraf, J. T.; Perera, A.; Lutz, J. J.; Bartlett, R. J. Single-reference coupled cluster theory for multi-reference problems. *J. Chem. Phys.* **2017**, *147*, na.
- (5) Cremer, D.; Filatov, M.; Polo, V.; Kraka, E.; Shaik, S. Implicit and Explicit Coverage of Multi-reference Effects by Density Functional Theory. *Int. J. Mol. Sci.* **2002**, *3*, 604–638.
- (6) Duan, C.; Liu, F.; Nandy, A.; Kulik, H. J. Data-Driven Approaches Can Overcome the Cost-Accuracy Trade-Off in Multireference Diagnostics. *J. Chem. Theory Comput.* **2020**, *16*, 4373–4387.
- (7) Jiang, W.; DeYonker, N. J.; Wilson, A. K. Multireference character for 3d transition-metal-containing molecules. *J. Chem. Theory Comput.* **2012**, *8*, 460–468.
- (8) Fogueri, U. R.; Kozuch, S.; Karton, A.; Martin, J. M. L. A simple DFT-based diagnostic for nondynamical correlation. *Theor. Chem. Acc.* **2013**, *132*, 1291.

- (9) Sprague, M. K.; Irikura, K. K. Quantitative estimation of uncertainties from wavefunction diagnostics. *Theor. Chem. Acc.* **2014**, 133, 1544.
- (10) Sears, J. S.; Sherrill, C. D. Assessing the Performance of Density Functional Theory for the Electronic Structure of Metal-Salens: The d2-Metals. *J. Phys. Chem. A* **2008**, *112*, 6741–6752.
- (11) Sears, J. S.; Sherrill, C. D. Assessing the Performance of Density Functional Theory for the Electronic Structure of Metal-Salens: The 3d0-Metals. *J. Phys. Chem. A* **2008**, *112*, 3466–3477.
- (12) Coe, J.; Murphy, P.; Paterson, M. Applying Monte Carlo configuration interaction to transition metal dimers: Exploring the balance between static and dynamic correlation. *Chem. Phys. Lett.* **2014**, *604*, 46–52.
- (13) Stanton, J. F.; Gauss, J.; Watts, J. D.; Lauderdale, W. J.; Bartlett, R. J. The ACES II program system. *Int. J. Quantum Chem.* **1992**, *44*, 879–894.
- (14) Perera, A.; Bartlett, R. J.; Sanders, B. A.; Lotrich, V. F.; Byrd, J. N. Advanced concepts in electronic structure (ACES) software programs. *J. Chem. Phys.* **2020**, *152*, na.
- (15) Lee, T. J.; Taylor, P. R. A diagnostic for determining the quality of single-reference electron correlation methods. *Int. J. Quantum Chem.* **1989**, *36*, 199–207.
- (16) Janssen, C. L.; Nielsen, I. M. New diagnostics for coupled-cluster and Møller–Plesset perturbation theory. *Chem. Phys. Lett.* **1998**, 290, 423–430.
- (17) Leininger, M. L.; Nielsen, I. M.; Crawford, T. D.; Janssen, C. L. A new diagnostic for open-shell coupled-cluster theory. *Chem. Phys. Lett.* **2000**, 328, 431–436.
- (18) Lee, T. J. Comparison of the T1 and D1 diagnostics for electronic structure theory: a new definition for the open-shell D1 diagnostic. *Chem. Phys. Lett.* **2003**, 372, 362–367.
- (19) Coe, J. P.; Paterson, M. J. Investigating Multireference Character and Correlation in Quantum Chemistry. J. Chem. Theory Comput. 2015, 11, 4189–4196.
- (20) Nielsen, I. M. B.; Janssen, C. L. Double-substitution-based diagnostics for coupled-cluster and Møller-Plesset perturbation theory. *Chem. Phys. Lett.* **1999**, *310*, 568–576.
- (21) Faulstich, F. M.; Kristiansen, H. E.; Csirik, M. A.; Kvaal, S.; Pedersen, T. B.; Laestadius, A. S-Diagnostic—An a Posteriori Error Assessment for Single-Reference Coupled-Cluster Methods. *J. Phys. Chem. A* 2023, 127, 9106—9120.
- (22) Tishchenko, O.; Zheng, J.; Truhlar, D. G. Multireference Model Chemistries for Thermochemical Kinetics. *J. Chem. Theory Comput.* **2008**, *4*, 1208–1219.
- (23) Jensen, H. J. A.; Jørgensen, P.; Ågren, H.; Olsen, J. Second-order Møller–Plesset perturbation theory as a configuration and orbital generator in multiconfiguration self-consistent field calculations. *J. Chem. Phys.* **1988**, *88*, 3834–3839.
- (24) Löwdin, P.-O. Quantum theory of many-particle systems. I. Physical interpretations by means of density matrices, natural spin-orbitals, and convergence problems in the method of configurational interaction. *Phys. Rev.* **1955**, *97*, 1474.
- (25) Ramos-Cordoba, E.; Salvador, P.; Matito, E. Separation of dynamic and nondynamic correlation. *Phys. Chem. Chem. Phys.* **2016**, 18, 24015–24023.
- (26) Ramos-Cordoba, E.; Matito, E. Local descriptors of dynamic and nondynamic correlation. *J. Chem. Theory Comput.* **2017**, *13*, 2705–2711.
- (27) Grimme, S.; Hansen, A. A Practicable Real-Space Measure and Visualization of Static Electron-Correlation Effects. *Angew. Chem., Int. Ed.* **2015**, *54*, 12308–12313.
- (28) Bauer, C. A.; Hansen, A.; Grimme, S. The fractional occupation number weighted density as a versatile analysis tool for molecules with a complicated electronic structure. *Chem. Eur. J.* **2017**, 23, 6150–6164.
- (29) Bartlett, R. J.; Park, Y. C.; Bauman, N. P.; Melnichuk, A.; Ranasinghe, D.; Ravi, M.; Perera, A. Index of multi-determinantal and multi-reference character in coupled-cluster theory. *J. Chem. Phys.* **2020**, *153*, na.

- (30) Legeza, Ö.; Sólyom, J. Optimizing the density-matrix renormalization group method using quantum information entropy. *Phys. Rev. B* **2003**, *68*, No. 195116.
- (31) Legeza, Ö.; Sólyom, J. Quantum data compression, quantum information generation, and the density-matrix renormalization-group method. *Phys. Rev. B: Condens. Matter Mater. Phys.* **2004**, 70, No. 205118.
- (32) Boguslawski, K.; Tecmer, P.; Barcza, G.; Legeza, Ö.; Reiher, M. Orbital Entanglement in Bond-Formation Processes. *J. Chem. Theory Comput.* **2013**, *9*, 2959–2973.
- (33) Stein, C. J.; Reiher, M. Measuring multi-configurational character by orbital entanglement. *Mol. Phys.* **2017**, *115*, 2110–2119.
- (34) Karton, A.; Rabinovich, E.; Martin, J. M. L.; Ruscic, B. W4 theory for computational thermochemistry: In pursuit of confident sub-kJ/mol predictions. *J. Chem. Phys.* **2006**, 125, No. 144108.
- (35) Karton, A.; Daon, S.; Martin, J. M. W4–11: A high-confidence benchmark dataset for computational thermochemistry derived from first-principles W4 data. *Chem. Phys. Lett.* **2011**, *510*, 165–178.
- (36) Schultz, N. E.; Zhao, Y.; Truhlar, D. G. Density Functionals for Inorganometallic and Organometallic Chemistry. *J. Phys. Chem. A* **2005**, *109*, 11127–11143.
- (37) Becke, A. D. Density-functional exchange-energy approximation with correct asymptotic behavior. *Phys. Rev. A* **1988**, 38, 3098.
- (38) Lee, C.; Yang, W.; Parr, R. G. Development of the Colle-Salvetti correlation-energy formula into a functional of the electron density. *Phys. Rev. B* **1988**, *37*, 785.
- (39) Adamo, C.; Barone, V. Toward reliable adiabatic connection models free from adjustable parameters. *Chem. Phys. Lett.* **1997**, 274, 242–250.
- (40) Martin, J. M. L.; Santra, G.; Semidalas, E. An exchange-based diagnostic for static correlation. AIP Conf. Proc. 2022, 2611, 020014.
- (41) Kesharwani, M. K.; Sylvetsky, N.; Köhn, A.; Tew, D. P.; Martin, J. M. L. Do CCSD and approximate CCSD-F12 variants converge to the same basis set limits? The case of atomization energies. *J. Chem. Phys.* **2018**, *149*, 154109.
- (42) Vogiatzis, K. D.; Ma, D.; Olsen, J.; Gagliardi, L.; de Jong, W. A. Pushing configuration-interaction to the limit: Towards massively parallel MCSCF calculations. *J. Chem. Phys.* **2017**, *147*, 184111.
- (43) White, S. R.; Martin, R. L. Ab initio quantum chemistry using the density matrix renormalization group. *J. Chem. Phys.* **1999**, *110*, 4127–4130.
- (44) Legeza, O.; Röder, J.; Hess, B. A. Controlling the accuracy of the density-matrix renormalization-group method: The dynamical block state selection approach. *Phys. Rev. B* **2003**, *67*, No. 125114.
- (45) Legeza, Ö.; Noack, R.; Sólyom, J.; Tincani, L. In *Computational Many-Particle Physics*, Lecture Notes in Physics; Fehske, H., Schneider, R., Weiße, A., Eds.; Springer: Berlin, Heidelberg, 2008; Vol. 739; pp 653–664.
- (46) Chan, G. K.-L.; Dorando, J. J.; Ghosh, D.; Hachmann, J.; Neuscamman, E.; Wang, H.; Yanai, T. In *Frontiers in Quantum Systems in Chemistry and Physics*, Progress in Theoretical Chemistry and Physics; Wilson, S., Grout, P. J., Maruani, J., Delgado-Barrio, G., Piecuch, P., Eds.; Springer: Netherlands, 2008; Vol. 18.
- (47) Yanai, T.; Kurashige, Y.; Ghosh, D.; Chan, G. K.-L. Accelerating convergence in iterative solution for large-scale complete active space self-consistent-field calculations. *Int. J. Quantum Chem.* **2009**, *109*, 2178–2190.
- (48) Marti, K. H.; Reiher, M. The Density Matrix Renormalization Group Algorithm in Quantum Chemistry. Z. Phys. Chem. 2010, 224, 583—500
- (49) Wouters, S.; Van Neck, D. The density matrix renormalization group for ab initio quantum chemistry. *European Physical Journal D* **2014**, *68*, na.
- (50) Szalay, Sz; Pfeffer, M.; Murg, V.; Barcza, G.; Verstraete, F.; Schneider, R.; Legeza, Ö Tensor product methods and entanglement optimization for ab initio quantum chemistry. *Int. J. Quantum Chem.* **2015**, *115*, 1342–1391.

- (51) Olivares-Amaya, R.; Hu, W.; Nakatani, N.; Sharma, S.; Yang, J.; Chan, G. K.-L. The ab-initio density matrix renormalization group in practice. *J. Chem. Phys.* **2015**, *142*, 034102.
- (52) Baiardi, A.; Reiher, M. The density matrix renormalization group in chemistry and molecular physics: Recent developments and new challenges. *J. Chem. Phys.* **2020**, *152*, 040903.
- (53) Cheng, Y.; Xie, Z.; Ma, H. Post-Density Matrix Renormalization Group Methods for Describing Dynamic Electron Correlation with Large Active Spaces. *J. Phys. Chem. Lett.* **2022**, *13*, 904–915.
- (54) Li, Z.; Li, J.; Dattani, N. S.; Umrigar, C. J.; Chan, G. K.-L. The electronic complexity of the ground-state of the FeMo cofactor of nitrogenase as relevant to quantum simulations. *J. Chem. Phys.* **2019**, 150, 024302.
- (55) Brabec, J.; Brandejs, J.; Kowalski, K.; Xantheas, S.; Legeza, ö; Veis, L. Massively parallel quantum chemical density matrix renormalization group method. *J. Comput. Chem.* **2021**, 42, 534–544.
- (56) Menczer, A.; van Damme, M.; Rask, A.; Huntington, L.; Hammond, J.; Xantheas, S. S.; Ganahl, M.; Legeza, Ö. Parallel implementation of the Density Matrix Renormalization Group method achieving a quarter petaFLOPS performance on a single DGX-H100 GPU node. *J. Chem. Theory Comput.* **2024**, 20, 8397–
- (57) Menczer, A.; Legeza, O. Tensor Network State Algorithms on AI Accelerators. *J. Chem. Theory Comput.* **2024**, *20*, 8897–8910.
- (58) Legeza, Ö.; Menczer, A.; Ganyecz, Á.; Werner, M. A.; Kapás, K.; Hammond, J.; Xantheas, S. S.; Ganahl, M.; Neese, F. Orbital optimization of large active spaces via AI-accelerators. *J. Chem. Theory Comput.* **2025**, *21*, 6545–6558.
- (59) Faulstich, F. M.; Máté, M.; Laestadius, A.; Csirik, M. A.; Veis, L.; Antalik, A.; Brabec, J.; Schneider, R.; Pittner, J.; Kvaal, S.; Legeza, Ö. Numerical and Theoretical Aspects of the DMRG-TCC Method Exemplified by the Nitrogen Dimer. *J. Chem. Theory Comput.* **2019**, 15, 2206–2220.
- (60) Barcza, G.; Noack, R. M.; Sólyom, J.; Legeza, Ö. Entanglement patterns and generalized correlation functions in quantum many-body systems. *Phys. Rev. B* **2015**, 92, No. 125140.
- (61) Boguslawski, K.; Tecmer, P. Orbital entanglement in quantum chemistry. *Int. J. Quantum Chem.* **2015**, *115*, 1289–1295.
- (62) Nowak, A.; Legeza, Ö.; Boguslawski, K. Orbital entanglement and correlation from pCCD-tailored coupled cluster wave functions. *J. Chem. Phys.* **2021**, *154*, na.
- (63) Khedkar, A.; Roemelt, M. Active Space Selection Based on Natural Orbital Occupation Numbers from n-Electron Valence Perturbation Theory. J. Chem. Theory Comput. 2019, 15, 3522–3536.
- (64) Fertitta, E.; Paulus, B.; Barcza, G.; Legeza, Ö. Investigation of metal-insulator-like transition through the ab initio density matrix renormalization group approach. *Phys. Rev. B* **2014**, *90*, No. 245129.
- (65) Ding, L.; Knecht, S.; Schilling, C. Quantum Information-Assisted Complete Active Space Optimization (QICAS). *J. Phys. Chem. Lett.* **2023**, *14*, 11022–11029.
- (66) Karton, A.; Sylvetsky, N.; Martin, J. M. L. W4–17: A diverse and high-confidence dataset of atomization energies for benchmarking high-level electronic structure methods. *J. Comput. Chem.* **2017**, *38*, 2063–2075.
- (67) Xu, X.; Zhang, W.; Tang, M.; Truhlar, D. G. Do practical standard coupled cluster calculations agree better than Kohn-Sham calculations with currently available functionals when compared to the best available experimental data for dissociation energies of bonds to 3 d transition metals? *J. Chem. Theory Comput.* **2015**, *11*, 2036–2052.
- (68) Welch, B. K.; Almeida, N. M. S.; Wilson, A. K. Super ccCA (sccCA): an approach for accurate transition metal thermochemistry. *Mol. Phys.* **2021**, *119*, e1963001.
- (69) Merriles, D. M.; Nielson, C.; Tieu, E.; Morse, M. D. Chemical bonding and electronic structure of the early transition metal borides: ScB, TiB, VB, YB, ZrB, NbB, LaB, HfB, TaB, and WB. *J. Phys. Chem. A* **2021**, *125*, 4420–4434.
- (70) Sun, X.; Wang, J.; Wu, Z. Chemical bonding and electronic structure of 4d-metal monosulfides. *JJ. Cluster Sci.* **2009**, 20, 525–534.

- (71) Anderson, A. B.; Hong, S. Y.; Smialek, J. Comparison of bonding in first transition-metal series: diatomic and bulk sulfides and oxides. *J. Phys. Chem.* **1987**, *91*, 4250–4254.
- (72) Gutsev, G. L.; Andrews, L.; Bauschlicher, C. W., Jr. Similarities and differences in the structure of 3 d-metal monocarbides and monoxides. *Theor. Chem. Acc.* **2003**, *109*, 298–308.
- (73) Denis, P. A.; Balasubramanian, K. Theoretical characterization of the low-lying electronic states of NbC. *J. Chem. Phys.* **2005**, *123*, na.
- (74) Suo, B.; Balasubramanian, K. Spectroscopic constants and potential energy curves of yttrium carbide (YC). *J. Chem. Phys.* **2007**, 126. na.
- (75) Denis, P. A.; Balasubramanian, K. Multireference configuration interaction study of the electronic states of ZrC. *J. Chem. Phys.* **2006**, 124, na.
- (76) Wang, J.; Manivasagam, S.; Wilson, A. K. Multireference character for 4d transition metal-containing molecules. *J. Chem. Theory Comput.* **2015**, *11*, 5865–5872.
- (77) Süß, D.; Huber, S. E.; Mauracher, A. On the impact of multi-reference character of small transition metal compounds on their bond dissociation energies. *J. Chem. Phys.* **2020**, *152*, na.
- (78) Aoto, Y. A.; de Lima Batista, A. P.; Köhn, A.; de Oliveira-Filho, A. G. S. How To Arrive at Accurate Benchmark Values for Transition Metal Compounds: Computation or Experiment? *J. Chem. Theory Comput.* **2017**, *13*, 5291–5316.
- (79) Purvis, G. D., III; Bartlett, R. J. A full coupled-cluster singles and doubles model: The inclusion of disconnected triples. *J. Chem. Phys.* **1982**, *76*, 1910–1918.
- (80) Raghavachari, K.; Trucks, G. W.; Pople, J. A.; Head-Gordon, M. A fifth-order perturbation comparison of electron correlation theories. *Chem. Phys. Lett.* **1989**, *157*, 479–483.
- (81) Dunning, J.; Thom, H. Gaussian basis sets for use in correlated molecular calculations. I. The atoms boron through neon and hydrogen. *J. Chem. Phys.* **1989**, *90*, 1007–1023.
- (82) Woon, D. E.; Dunning, T. H. Gaussian basis sets for use in correlated molecular calculations. III. The atoms aluminum through argon. *J. Chem. Phys.* **1993**, *98*, 1358–1371.
- (83) Balabanov, N. B.; Peterson, K. A. Systematically convergent basis sets for transition metals. I. All-electron correlation consistent basis sets for the 3d elements Sc–Zn. *J. Chem. Phys.* **2005**, *123*, 064107.
- (84) Mester, D.; Nagy, P. R.; Csóka, J.; Gyevi-Nagy, L.; Szabó, P. B.; Horváth, R. A.; Petrov, K.; Hégely, B.; Ladóczki, B.; Samu, G.; et al. Overview of Developments in the MRCC Program System. *J. Phys. Chem. A* 2025, *129*, 2086–2107.
- (85) Lu, T.; Chen, F. Multiwfn: A multifunctional wavefunction analyzer. *J. Comput. Chem.* **2012**, 33, 580-592.
- (86) Pipek, J.; Mezey, P. G. A fast intrinsic localization procedure applicable for ab initio and semiempirical linear combination of atomic orbital wave functions. *J. Chem. Phys.* **1989**, *90*, 4916–4926.
- (87) Legeza, O.; Veis, L.; Mosoni, T. *QC-DMRG-Budapest*, a program for quantum chemical DMRG calculations, 2021.
- (88) Barcza, G.; Legeza, Ö.; Marti, K. H.; Reiher, M. Quantum-information analysis of electronic states of different molecular structures. *Phys. Rev. A* **2011**, 83, No. 012508.
- (89) Neese, F.; Wennmohs, F.; Becker, U.; Riplinger, C. The ORCA quantum chemistry program package. *J. Chem. Phys.* **2020**, *152*, 224108.
- (90) Perdew, J. P.; Burke, K.; Ernzerhof, M. Generalized gradient approximation made simple. *Phys. Rev. Lett.* **1996**, *77*, 3865.
- (91) Adamo, C.; Barone, V. Toward reliable density functional methods without adjustable parameters: The PBE0 model. *J. Chem. Phys.* **1999**, *110*, 6158–6170.
- (92) Hollander, M.; Wolfe, D. A.; Chicken, E. Nonparametric Statistical Methods; John Wiley & Sons, 2013.
- (93) Xu, X.; Soriano-Agueda, L.; López, X.; Ramos-Cordoba, E.; Matito, E. All-Purpose Measure of Electron Correlation for Multi-reference Diagnostics. *J. Chem. Theory Comput.* **2024**, *20*, 721–727.

- (94) Xu, X.; Soriano-Agueda, L.; López, X.; Ramos-Cordoba, E.; Matito, E. How many distinct and reliable multireference diagnostics are there? *I. Chem. Phys.* **2025**, *162*, 124102.
- (95) Weflen, K. E.; Bentley, M. R.; Thorpe, J. H.; Franke, P. R.; Martin, J. M.; Matthews, D. A.; Stanton, J. F. Exploiting a Shortcoming of Coupled-Cluster Theory: The Extent of Non-Hermiticity as a Diagnostic Indicator of Computational Accuracy. *J. Phys. Chem. Lett.* **2025**, *16*, 5121–5127.
- (96) Hait, D.; Tubman, N. M.; Levine, D. S.; Whaley, K. B.; Head-Gordon, M. What levels of coupled cluster theory are appropriate for transition metal systems? A study using near-exact quantum chemical values for 3d transition metal binary compounds. *J. Chem. Theory Comput.* **2019**, *15*, 5370–5385.
- (97) Cheng, L.; Gauss, J.; Ruscic, B.; Armentrout, P. B.; Stanton, J. F. Bond dissociation energies for diatomic molecules containing 3d transition metals: benchmark scalar-relativistic coupled-cluster calculations for 20 molecules. *J. Chem. Theory Comput.* **2017**, *13*, 1044–1056.
- (98) Fang, Z.; Vasiliu, M.; Peterson, K. A.; Dixon, D. A. Prediction of bond dissociation energies/heats of formation for diatomic transition metal compounds: CCSD (T) works. *J. Chem. Theory Comput.* **2017**, *13*, 1057–1066.

